Simulation of the 3D viscoelastic free surface flow by a parallel corrected particle scheme*

Jin-Lian Ren(任金莲)† and Tao Jiang(蒋涛)

Department of Mathematics, Yangzhou University, Yangzhou 225002, *China*

(Received 6 August 2015; revised manuscript received 21 September 2015; published online 20 December 2015)

In this work, the behavior of the three-dimensional (3D) jet coiling based on the viscoelastic Oldroyd-B model is investigated by a corrected particle scheme, which is named the smoothed particle hydrodynamics with corrected symmetric kernel gradient and shifting particle technique (SPH_CS_SP) method. The accuracy and stability of SPH_CS_SP method is first tested by solving Poiseuille flow and Taylor–Green flow. Then the capacity for the SPH_CS_SP method to solve the viscoelastic fluid is verified by the polymer flow through a periodic array of cylinders. Moreover, the convergence of the SPH_CS_SP method is also investigated. Finally, the proposed method is further applied to the 3D viscoelastic jet coiling problem, and the influences of macroscopic parameters on the jet coiling are discussed. The numerical results show that the SPH_CS_SP method has higher accuracy and better stability than the traditional SPH method and other corrected SPH method, and can improve the tensile instability.

Keywords: SPH, corrected scheme, shifting particle technique, jet coiling

PACS: 02.70.–c, 47.11.–j, 47.85.md **DOI:** 10.1088/1674-1056/25/2/020204

1. Introduction

The complex jet coiling phenomena,[1] although they play an important role in many industrial processes, such as extrusion, and container filling with polymers, are still less well understood in terms of fundamental fluid dynamics. In order to predict the complex rheological phenomena in a real three-dimensional (3D) viscoelastic jet buckling process, a number of grid-based numerical methods have been proposed, such as the finite difference method (FDM), finite element method (FEM), finite volume method (FVM), etc. The mesh-based methods mentioned above have been applied to many fluid mechanic fields.

However, these grid-based methods also suffer numerical difficulties, such as severe mesh distortion, and the expensive cost in the mesh generation process. As one may expect, the various mesh-free methods[2–4] in a Lagrangian framework have been proposed to solve the fluid dynamic problems, such as the smoothed particle hydrodynamics (SPH) method,[4,5] element-free Galerkin (EFG) method,[3] reproducing kernel particle method (RKPM),[6–8] and so on.

The SPH method[5] is a pure meshless method which employs Lagrangian description of motion. Recently, the SPH method has been extensively applied to the fluid dynamic areas due to its merits, such as viscous flows,[9] free surface flows,[5,10,11] incompressible fluids,[12,13] multi-phase flows,[14] and non-Newtonian fluid flows.[13,15] However, the application of the SPH method to the viscoelastic fluid mainly focuses on the two-dimensional (2D) viscoelastic jet buckling, and the application of the SPH method to the 3D viscoelastic jet coiling has received a little attention recently. The reason is that the SPH method usually suffers two major drawbacks, that is, the particle inconsistency[16,17] for uninformed particle distributions/near the boundary domain and the numerical/tensile instability.[18] In order to restore the consistency of the kernel and gradient particle approximations of SPH, some improved SPH methods based on the Taylor series expansion have been proposed, such as the corrected smoothed particle hydrodynamics method (CSPM),[19] finite particle method (FPM),[11,20] the modified SPH (MSPH) method,[21] and the symmetric SPH (SSPH) method.[22] Although these improved methods have higher accuracy than the traditional SPH (TSPH) method, some disadvantages still exist and make it more difficult to be extended to the complex fluid dynamic problems,[22] the choice of the kernel function is limited for solving the partial differential equations (PDEs) with higher derivatives; the local matrix is asymmetric, which can cause numerical instability; its computational efficiency is lower than that of TSPH, such as the MSPH method and SSPH method. Therefore, a corrected kernel gradient scheme[23] has been introduced into the TSPH method and extensively applied to Newtonian fluid[24,25] in recent years. However, the corrected kernel gradient scheme has been rarely extended to simulate the viscoelastic jet buckling, especially the 3D simulations of the viscoelastic jet coiling.

In the present paper, the 3D viscoelastic jet coiling process based on the Oldroyd-B model is simulated and analyzed

*Project supported by the Natural Science Foundation of Jiangsu Province, China (Grant Nos. BK20130436 and BK20150436) and the Natural Science Foundation of the Higher Education Institutions of Jiangsu Province, China (Grant No. 15KJB110025).

†Corresponding author. E-mail: rjl20081223@126.com

© 2016 Chinese Physical Society and IOP Publishing Ltd

by a parallel coupled corrected particle scheme named the SPH_CS_SP (SPH with a corrected symmetric kernel gradient scheme and shifting particle technique) method. Some special phenomena of the 3D jet coiling are observed and the physical explanations of these complex phenomena are also analyzed. The proposed particle method combines three improved concepts, that is, introducing the incompressible condition in the momentum equation to achieve better robustness,[26] extending the corrected symmetric kernel gradient scheme[27] to further improve the numerical accuracy and employing the shifting particle technique to overcome the tensile instability.[28] It should be noted that the main difference between the proposed SPH_CS_SP method and other improved SPH methods lies in the following respects: (i) the obtained discretized form of momentum equation is different from those in Refs. [24] and [25]; (ii) the shifting particle technique is first applied to the viscoelastic fluid flows; (iii) the presented corrected SPH method is different from the particle methods in Refs. [24] and [29], which have not been extended to simulate the 3D polymer free surface flow.

The rest of this paper is organized as follows. The governing equations and the viscoelastic constitutive model are introduced in Section 2. In Section 3, the details of the proposed SPH_CS_SP scheme for the viscoelastic fluid are described. The accuracy and robustness of SPH_CS are tested by simulating the Poiseuille flow in Section 4. Moreover, the necessity of enforcing the shifting particles technique is also investigated by simulating the Taylor–Green flow in Section 4. In Section 5, the capacity for SPH_CS_SP to simulate the viscoelastic flow is verified by the polymer flow around a periodic array of cylinders. In Section 6, the proposed particle method with MPI parallelization technique is extended to simulate the 3D viscoelastic jet coiling problem in the filling process. Some conclusions are drawn from the present study in Section 7.

2. Governing equations based on the Oldroyd-B model

In the 3D Lagrangian frame, the governing equations of a weakly compressible fluid can be described as follows:

$$\frac{\mathrm{d}\rho}{\mathrm{d}t} = -\rho\nabla\cdot\boldsymbol{v}, \tag{1}$$

$$\frac{\mathrm{d}\boldsymbol{v}}{\mathrm{d}t} = \frac{1}{\rho}\nabla\cdot\boldsymbol{\sigma} + \boldsymbol{F}, \tag{2}$$

where $\boldsymbol{v} = (u, v, w)$ is the velocity vector, ρ is the fluid density, t is the time, $\boldsymbol{F}$ is the body force, and $\mathrm{d}/\mathrm{d}t$ is the material derivative $\mathrm{d}/\mathrm{d}t = \partial/\partial t + \boldsymbol{v}\cdot\nabla$. The Cauchy stress tensor $\boldsymbol{\sigma}$ in Eq. (2) is decomposed into the ordinary isotropic pressure p and extra stress tensor $\boldsymbol{T}_\mathrm{o}$:

$$\boldsymbol{\sigma} = -p\boldsymbol{I} + \boldsymbol{T}_\mathrm{o}, \tag{3}$$

where $\boldsymbol{I}$ refers to the identity matrix.

In this paper, we choose the Oldroyd-B model as the constitutive equation, which represents the basic viscoelastic fluid and shows complex rheological behavior of polymer flow. The extra stress tensor $\boldsymbol{T}_\mathrm{o}$ for the Oldroyd-B model is usually decomposed into viscous $2\eta_\mathrm{s}\boldsymbol{D}$ and polymeric contributions $\boldsymbol{\tau}$:

$$\boldsymbol{T}_\mathrm{o} = 2\eta_\mathrm{s}\boldsymbol{D} + \boldsymbol{\tau}, \tag{4}$$

$$\boldsymbol{\tau} + \lambda_{0\mathrm{b}}\overset{\nabla}{\boldsymbol{\tau}} + = 2\eta_\mathrm{p}\boldsymbol{D}, \tag{5}$$

where the rate of deformation tensor $\boldsymbol{D} = \frac{1}{2}\left(\nabla\boldsymbol{v} + (\nabla\boldsymbol{v})^\mathrm{T}\right)$, $\lambda_{0\mathrm{b}}$ is the relaxation time, and the symbol "$\overset{\nabla}{\cdot}$" represents the following upper-convected derivative

$$\overset{\nabla}{\boldsymbol{\tau}} = \frac{\mathrm{d}\boldsymbol{\tau}}{\mathrm{d}t} - \boldsymbol{\tau}\cdot(\nabla\boldsymbol{v}) - (\nabla\boldsymbol{v})^\mathrm{T}\cdot\boldsymbol{\tau}. \tag{6}$$

Moreover, some parameters are introduced, that is, the total viscosity $\eta = \eta_\mathrm{s} + \eta_\mathrm{p}$, the ratio of Newtonian and polymeric viscosity $\beta_0 = \eta_\mathrm{s}/(\eta_\mathrm{s} + \eta_\mathrm{p})$, the Reynolds number $Re = (\rho UL)/\eta$, and the Weissenberg number $We = (\lambda_{0\mathrm{b}}U)/L$, where U and L represent the characteristic velocity and length, respectively.

Like many previous studies,[4,9] here we also treat the incompressible flows as a slightly compressible fluid by a suitable equation of state, that is[10]

$$p(\rho) = c^2(\rho - \rho_0), \tag{7}$$

where c is the speed of sound, and ρ_0 is the reference density. It can be shown that the density variation is proportional to the Mach number M ($M \equiv V/c$, where V is a typical reference velocity).[4,9]

3. SPH_CS_SP method for viscoelastic fluid

In order to accurately simulate the viscoelastic fluid flow, a new corrected particle scheme is proposed. It mainly combines three different improvements, that is, introducing the incompressible condition in the momentum equation to achieve better robustness,[26] applying the corrected symmetric kernel gradient method[29] to the discrete form of the first derivative to improve the numerical accuracy, and employing the shifting particle technique to overcome the tensile instability.[25,26,28]

3.1. Traditional SPH (TSPH) scheme

As is well known, in the traditional SPH method, the particle approximation for a function f and its first derivative at particle i can be written as[4,5]

$$f_i = \sum_j \frac{m_j}{\rho_j} f_j W_{ij}, \tag{8}$$

$$\left(\frac{\partial f}{\partial \boldsymbol{r}_i}\right) = \sum_j \frac{m_j}{\rho_j}(f_j - f_i)\frac{\partial W_{ij}}{\partial \boldsymbol{r}_i}, \tag{9}$$

where m_j and ρ_j are the mass and the density of the neighbor particle j located in the support domain of particle i,

respectively, W is the kernel function which usually satisfies some properties,[4] $W_{ij}=W\left(\left|\boldsymbol{r}_i-\boldsymbol{r}_j\right|,h\right)$, $\partial W_{ij}/\partial \boldsymbol{r}_i=\partial W\left(\left|\boldsymbol{r}_i-\boldsymbol{r}_j\right|,h\right)/\partial \boldsymbol{r}_i$, h being the smoothing length.

The kernel function is related not only to the accuracy but also to the efficiency and the stability of the resulting algorithm. As shown in Ref. [29], the Wendland function can produce more accurate results than the common spline kernel functions. So the following quintic Wendland kernel function is adopted:

$$\begin{aligned} W_{ij} &= W(r,h) \\ &= w_0\begin{cases}[1-(r/h)]^4\left[(4r/h)+1\right], & 0\le r/h<1,\\ 0, & r/h\ge 1,\end{cases} \end{aligned} \tag{10}$$

where the $r=\left|\boldsymbol{r}_i-\boldsymbol{r}_j\right|$ and the normalization factor w_0 is $7/\left(\pi h^2\right)$.

According to Eq. (9), the discrete scheme of the continuity equation (1) is

$$\left(\frac{\mathrm{d}\rho}{\mathrm{d}t}\right)_i=\rho_i\sum_j\frac{m_j}{\rho_j}(v_i^\beta-v_j^\beta)\frac{\partial W_{ij}}{\partial x_i^\beta}. \tag{11}$$

Considering the discrete gradient scheme

$$\frac{\partial f}{\partial \boldsymbol{r}_i}=\sum_j\frac{m_j}{\rho_j}f_j\frac{\partial W_{ij}}{\partial \boldsymbol{r}_i}$$

and the following identity:

$$\frac{1}{\rho}\frac{\partial\sigma^{\alpha\beta}}{\partial x^\beta}=\frac{\partial\left(\sigma^{\alpha\beta}/\rho\right)}{\partial x^\beta}+\frac{\sigma^{\alpha\beta}}{\rho^2}\frac{\partial\rho}{\partial x^\beta},$$

we can obtain the conventional discretized scheme of the momentum equation (2), which is

$$\left(\frac{\mathrm{d}v^\alpha}{\mathrm{d}t}\right)_i=\sum_j m_j\left(\frac{\sigma_i^{\alpha\beta}}{\rho_i^2}+\frac{\sigma_j^{\alpha\beta}}{\rho_j^2}\right)\frac{\partial W_{ij}}{\partial x_i^\beta}+F^\alpha, \tag{12}$$

where v^β is the β-th component of the fluid velocity, $\sigma^{\alpha\beta}$ is the (α,β)-th component of the total stress tensor, and x^β is the component of spatial coordinate.

The particle discretized scheme of total stress equation (3) can be defined as

$$\sigma_i^{\alpha\beta}=-p\delta^{\alpha\beta}+\beta_0\eta\left(\kappa_i^{\alpha\beta}+\kappa_i^{\beta\alpha}\right)+\left(\tau^{\alpha\beta}\right)_i, \tag{13}$$

where

$$\kappa_i^{\alpha\beta}=\left(\frac{\partial v^\alpha}{\partial x^\beta}\right)_i=\sum_j\frac{m_j}{\rho_j}(v_j^\alpha-v_i^\alpha)\frac{\partial W_{ij}}{\partial x_i^\beta}, \tag{14}$$

and the discretized scheme of the constitutive equation (5) is

$$\begin{aligned}\left(\frac{\mathrm{d}\tau^{\alpha\beta}}{\mathrm{d}t}\right)_i &= \kappa_i^{\alpha\gamma}\tau_i^{\gamma\beta}+\kappa_i^{\beta\gamma}\tau_i^{\gamma\alpha}-\frac{1}{\lambda_{0\mathrm{b}}}\tau_i^{\alpha\beta} \\ &\quad+\frac{(1-\beta_0)\eta}{\lambda_{0\mathrm{b}}}\left(\kappa_i^{\alpha\beta}+\kappa_i^{\beta\alpha}\right).\end{aligned} \tag{15}$$

3.2. SPH_CS_SP method

The TSPH discretized formulas (11)–(15) for the viscoelastic Oldroyd-B fluid are directly derived from the TSPH discrete formula for the viscous fluid.[15] As is well known, the TSPH formula for the viscous flow suffers low numerical accuracy and instability, especially for the non-uniform distributed particles and boundary particles (see Refs. [4], [11], and [16]). Moreover, the influence of elastic stress on the numerical simulations of viscoelastic fluid flow is also significant, which easily leads to the instability of numerical schemes for the viscoelastic flow. Therefore, in order to obtain a particle method that possesses higher accuracy and better stability, we introduce three improvements[27,28] into the TSPH formulas (11)–(15). The improvements are described in detail as follows.

Firstly, introducing the incompressible condition into momentum equation (2) leads to

$$\frac{\mathrm{d}\boldsymbol{v}}{\mathrm{d}t}=-\frac{1}{\rho}\nabla p+\frac{1}{\rho}\left(\eta_\mathrm{s}\nabla^2\boldsymbol{v}+\nabla\cdot\boldsymbol{\tau}\right)+\boldsymbol{F}, \tag{16}$$

and considering the discrete scheme of the Laplace operator,[13] the following discretized scheme of the momentum equation (16) is obtained

$$\begin{aligned}\left(\frac{\mathrm{d}v^\alpha}{\mathrm{d}t}\right)_i &= -\sum_j m_j\left(\frac{p_i}{\rho_i^2}+\frac{p_j}{\rho_j^2}\right)\frac{\partial W_{ij}}{\partial x_i^\alpha} \\ &\quad+\sum_j\frac{4m_j\beta_0\left(\eta_i+\eta_j\right)v_{ij}^\alpha}{\left(\rho_i+\rho_j\right)^2\left(\left|\boldsymbol{r}_{ij}\right|^2+0.01h^2\right)}x_{ij}^\beta\frac{\partial W_{ij}}{\partial x_i^\beta} \\ &\quad+\sum_j m_j\left(\frac{\tau_i^{\alpha\beta}}{\rho_i^2}+\frac{\tau_j^{\alpha\beta}}{\rho_j^2}\right)\frac{\partial W_{ij}}{\partial x_i^\beta}+F^\alpha,\end{aligned} \tag{17}$$

where $\boldsymbol{r}_{ij}=\boldsymbol{r}_i-\boldsymbol{r}_j$.

Secondly, the corrected symmetric kernel gradient scheme[27] and the Taylor expansion concept[18] are also applied to the first-order derivative and the elastic stress part of Eq. (12) to restore the particle approximation and consistency and improve the numerical accuracy and stability of TSPH method, respectively. Thus the following corrected symmetric SPH (SPH_CS) scheme for the viscoelastic Oldroyd-B fluid is obtained:

$$\left(\frac{\mathrm{d}\rho}{\mathrm{d}t}\right)_i=-\rho_i\sum_j\frac{m_j}{\rho_j}(v_j^\beta-v_i^\beta)\frac{\partial\tilde{W}_{ij}^{\mathrm{CS}}}{\partial x_i^\beta}, \tag{18}$$

$$\begin{aligned}\left(\frac{\mathrm{d}v^\alpha}{\mathrm{d}t}\right)_i &= -\sum_j m_j\left(\frac{p_i}{\rho_i^2}+\frac{p_j}{\rho_j^2}\right)\frac{\partial\tilde{W}_{ij}^{\mathrm{CS}}}{\partial x_i^\alpha} \\ &\quad+\sum_j\frac{4m_j\beta_0\left(\eta_i+\eta_j\right)v_{ij}^\alpha}{\left(\rho_i+\rho_j\right)^2\left(\left|\boldsymbol{r}_{ij}\right|^2+0.01h^2\right)}x_{ij}^\beta\frac{\partial\tilde{W}_{ij}^{\mathrm{CS}}}{\partial x_i^\beta} \\ &\quad+\sum_j\frac{m_j}{\rho_i\rho_j}\left(\tau_j^{\alpha\beta}-\tau_i^{\alpha\beta}\right)\frac{\partial\tilde{W}_{ij}^{\mathrm{CS}}}{\partial x_i^\beta}+F^\alpha,\end{aligned} \tag{19}$$

$$\tilde{\kappa}_i^{\alpha\beta}=\left(\frac{\partial v^\alpha}{\partial x^\beta}\right)_i=\sum_j\frac{m_j}{\rho_j}(v_j^\alpha-v_i^\alpha)\frac{\partial\tilde{W}_{ij}^{\mathrm{CS}}}{\partial x_i^\beta}, \tag{20}$$

where

$$\begin{pmatrix}\partial\tilde{W}_{ij}^{\mathrm{CS}}/\partial x_i\\ \partial\tilde{W}_{ij}^{\mathrm{CS}}/\partial y_i\\ \partial\tilde{W}_{ij}^{\mathrm{CS}}/\partial z_i\end{pmatrix}=(A^s)^{-1}\begin{pmatrix}x_{ji}W_{ij}\\ y_{ji}W_{ij}\\ z_{ji}W_{ij}\end{pmatrix},$$

$$A^s = \begin{pmatrix} \sum_{j=1}^{N} \frac{m_j}{\rho_j} x_{ji}x_{ji}W_{ij} & \sum_{j=1}^{N} \frac{m_j}{\rho_j} y_{ji}x_{ji}W_{ij} & \sum_{j=1}^{N} \frac{m_j}{\rho_j} z_{ji}x_{ji}W_{ij} \\ \sum_{j=1}^{N} \frac{m_j}{\rho_j} x_{ji}y_{ji}W_{ij} & \sum_{j=1}^{N} \frac{m_j}{\rho_j} y_{ji}y_{ji}W_{ij} & \sum_{j=1}^{N} \frac{m_j}{\rho_j} z_{ji}y_{ji}W_{ij} \\ \sum_{j=1}^{N} \frac{m_j}{\rho_j} x_{ji}z_{ji}W_{ij} & \sum_{j=1}^{N} \frac{m_j}{\rho_j} y_{ji}z_{ji}W_{ij} & \sum_{j=1}^{N} \frac{m_j}{\rho_j} z_{ji}z_{ji}W_{ij} \end{pmatrix}. \tag{21}$$

It should be noted that the discretized form Eq. (19) for the momentum equation is different from that in Ref. [27], especially the corrected discretized form of polymer elastic stress in accordance with the Taylor series concept in Eq. (19). Also, the local matrix equation (21) is different from those in Refs. [24] and [25].

At the end of each time-step, the position of each particle is updated by

$$\frac{\mathrm{d}x_i^\alpha}{\mathrm{d}t} = v_i^\alpha. \tag{22}$$

Finally, a shifting particle technique,[28] which is applied only to the viscous fluid now, is extended to the viscoelastic fluid to obtain a uniform particle distribution and further improve the tensile instability. Next, we describe the shifting particle technique in detail.

After each time-step, the position of particle i is shifted according to the following formula:

$$\boldsymbol{r}_i' = \boldsymbol{r}_i + \xi U_{\max} \Delta t \bar{r}_i, \tag{23a}$$

where $\boldsymbol{r}_i'$ is the particle position after shifting, ξ is a constant that ranges from 0.01 to 0.1, $U_{\max}$ is the maximum particle velocity or the characteristic velocity of flow, Δt is the time-step, and the shifting vector is defined as

$$\bar{r}_i = \sum_j^{M_i} \left(\bar{r}_i^2 / r_{ij}^2\right)(\boldsymbol{r}_{ij}/r_{ij}), \tag{23b}$$

where M_i is the number of neighboring particles of the particle i, $r_{ij} = \left|\boldsymbol{r}_{ij}\right|$, and $\bar{r}_i = \sum_j^{M_i} r_{ij}$ is the average particle spacing in the neighborhood of i. The shifting vector $\bar{r}_i = 0$ when the fluid particles near the particle i are uniformly distributed.

For simplicity, the method that combines the three different improvements is named the SPH_CS_SP method.

3.3. Boundary treatment

In the SPH simulations, the boundary treatment is an important problem. Next, we will describe the boundary treatment used in this paper.

For the solid boundary, the approach of two types of virtual particles[27] is extended to simulating the viscoelastic fluid flows in this paper. The first type of particle is placed on the solid wall, namely "wall particle". The pressure and the components of the velocity of the wall particle i are calculated according to the following formula:

$$\boldsymbol{s}_i = \sum_j \boldsymbol{s}_j (2h - r_{ij}) / \sum_j (2h - r_{ij}), \tag{24}$$

where $\boldsymbol{s} = (P_W, u_w^\alpha, \tau_W)$, j represents the indices of the fluid particles within the influence domain of the boundary particle i.

The second type of particle, called "dummy particle", is placed just outside the solid wall, in a way which is similar to how the wall particle is located. In general, three layers of dummy particles are chosen. The pressure, velocity and extra stress tensor on the dummy particles are computed by the following formula:

$$\boldsymbol{S}_D = \boldsymbol{S}_F + \left(1 + \frac{d_D}{d_F}\right)(\boldsymbol{S}_W - \boldsymbol{S}_F), \tag{25}$$

where $\boldsymbol{S}$ represents the vector of variables $\left(p_D, u_D^\alpha, \tau_D^{\alpha\beta}\right)$, d_D and d_F are the normal distances of the dummy particles D and the fluid particle F to solid wall, respectively. To specify the values of $\boldsymbol{S}_F$, the interpolation formula (24) is applied again. For the periodic boundary, we adopt an established molecular dynamics routine with SPH particles crossing the boundary being re-inserted on the opposite side of the simulation box.[15]

3.4. Time integration scheme

In order to solve the system of ordinary differential equations (15), (18), (19), and (22), we choose the predictor–corrector scheme,[27] which has second-order accuracy and better stability. The predictor step consists of a Eulerian explicit evaluation of all quantities for each particle

$$\tilde{\boldsymbol{K}}_i^{n+1} = \boldsymbol{K}_i^n + \frac{\Delta t}{2} \boldsymbol{\Gamma}_i^n, \tag{26a}$$

where $\boldsymbol{K}_i$ represents the vector of the unknown variables $(\rho_i, u_i^\alpha, \tau_i^\alpha, x_i^\alpha)$ and $\boldsymbol{\Gamma}_i$ denotes the vector of the right-hand side of each of Eqs. (15), (18), (19), and (22). In the corrected step, the updated value of at the end of each time step is given by

$$\boldsymbol{K}_i^{n+1} = \boldsymbol{K}_i^n + \frac{\Delta t}{2}\left(\boldsymbol{\Gamma}_i^n + \tilde{\boldsymbol{\Gamma}}_i^{n+1}\right). \tag{26b}$$

As is well known, the time-step and space-step must satisfy the well-known Courant–Friedrichs–Lewy (CFL) condition for ensuring the numerical stability. According to

Refs. [14] and [30], we may choose the following stability condition:

$$\Delta t \leq \min\left[0.25\frac{h}{c}, 0.125\frac{h^2}{\upsilon_0}\right], \tag{26c}$$

where $\upsilon_0 = \eta/\rho_0$ is the kinematic viscosity.

4. Valid test for the SPH_CS_SP method

4.1. Accuracy and the stability of SPH_CS_CP method

In this section, the Poiseuille flow of Oldroyd-B fluid is simulated by SPH_CS_CP method to test the capacity for the proposed SPH_CS method to solve the transient viscoelastic fluid, and the numerical results are compared with those obtained by TSPH method and the analytical solutions. It should be noted that the tensile instability does not exist in the simulations of the Poiseuille flow, and the shifting particle technique is not considered in this subsection.

Figure 1 shows the velocity u and the stress τ^{xy} profiles at different times for the Poiseuille flow of Oldroyd-B fluid. Here the uniformed particle distribution is used. The employed non-dimensional parameters are as follows: two parallels are located at $y = 0$ and $y = 1$, the density $\rho_0 = 1$, the characteristic velocity $U = FL_0^2/8\upsilon_0$, the ratio of viscosity $\beta_0 = 0.3$, the kinematic viscosity $\upsilon_0 = 2$, the body force $F = 1$, $Re \approx 0.03$, the relaxation time, $\lambda_{ob} = 0.2, 4$ which correspond to $We = 0.012, 0.25$, respectively, the sound speed $c = 10U_{max}$, the time-step $\Delta t = 10^{-4}$, the smoothing length $h = 2.5d_0$ (d_0 is the initial distance between two particles), the number of fluid particles is 31×61.

Table 1 gives the relative L_1-error norms of the velocity profiles in Fig. 1(a). The relative L_1-error norm is defined as

$$E_1(u) = \left(\sum_{j=1}^{N_y} |\tilde{u}_j - u_j|\right) \Big/ \left(\sum_{j=1}^{N_y} |u_j|\right),$$

where N_y denotes the particle number along the y axis, $\tilde{u}_j$ and u_j are the numerical and the analytical solution at position x_j, respectively.

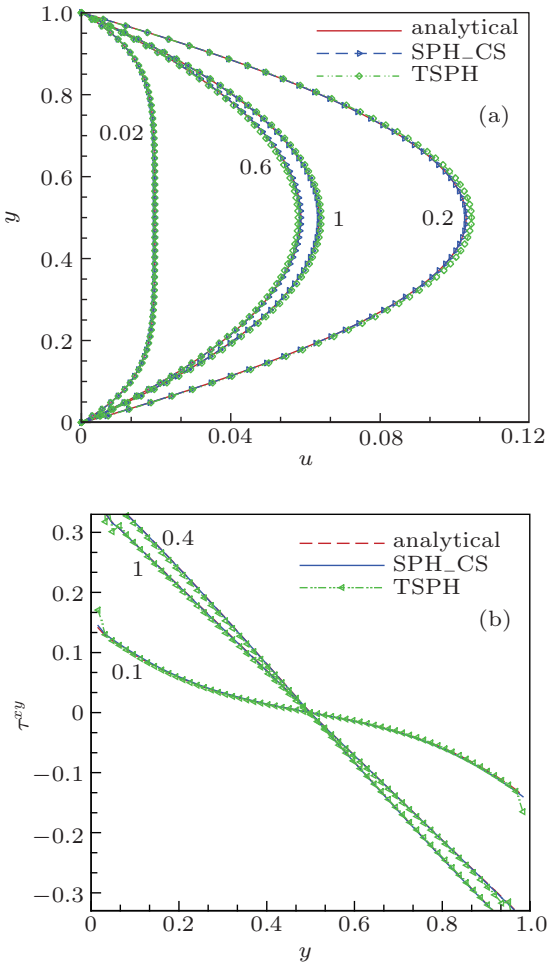


Fig. 1. (color online) Results for the Oldroyd-B fluid at different times with $Re \approx 0.03$: (a) $u(y)$; (b) $\tau^{xy}(y)$.

From Fig. 1 and Table 1, we can observe that the SPH_CS results are much closer to the analytical solutions than the TSPH results, and the SPH_CS method has faster numerical convergence than the TSPH method for solving the viscoelastic fluid flow under the uniformed particle distributions. It is worth noting that the shear elastic stress obtained by the TSPH method has small oscillation near the boundary, which leads to the numerical instability varying with time. Meanwhile, the overshooting phenomenon can be observed in the Oldroyd-B fluid flow.

Table 1. Relative L_1-error norm of the velocity profiles for the case of Fig. 1(a).

Time t	Particle number N_y	L_1-error norm (TSPH)	L_1-error norm (SPH_CS)
0.05	21	0.0321623	0.0240623
	41	0.01222612	0.00822612
	81	0.00811651	0.000923651
0.5	21	0.0873986	0.0275686
	41	0.01316113	0.00921113
	81	0.00872631	0.00258731
1	21	0.7921751	0.0387751
	41	0.11231073	0.03041073
	81	0.00922073	0.00401073

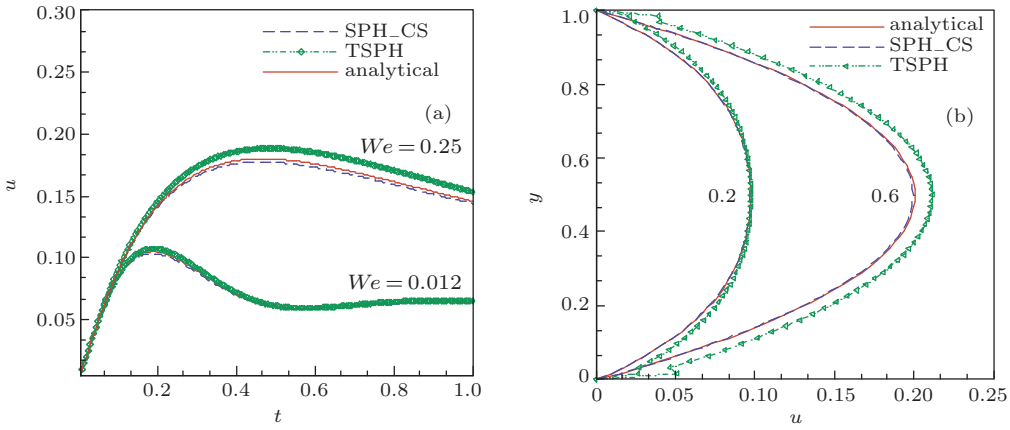


Fig. 2. (color online) Velocity profiles for the Poiseuille flow of Oldroyd-B fluid with different values of *We* and *Re*: (a) $Re \approx 0.03$, $u(y = 0.5)$; (b) $Re = 1$, $u(y)$.

Figure 2 shows the velocity profiles for the Poiseuille flow of Oldroyd-B fluid with different values of *We* and *Re*. In Fig. 2(a), the parameters are the same as those in Fig. 1. In Fig. 2(b), the parameters are the same as those in Fig. 1 except that $\upsilon_0 = 0.25$, $F = 0.5$, $Re = 1$, $\lambda_{ob} = 0.04$, and $We = 0.01$. From Fig. 2, it can be observed that the velocity overshooting behavior becomes more evident and the accuracy of SPH_CS results becomes higher than that of TSPH results with increasing Weissenberg number (Fig. 2(a)). With increasing Reynolds number, the TSPH solutions are much further from the analytical ones with time going by and they appear unstable near boundary domain about $t = 0.6$ (see Fig. 2(b)).

The numerical results in Figs. 1 and 2 show that the SPH_CS has higher accuracy and better robustness than the TSPH for simulating the viscoelastic fluid flow, especially with the larger Weissenberg number or Reynolds number, and the overshooting phenomenon of velocity obtained by the SPH_CS method is more accurate than that obtained by the TSPH method, especially for the larger Weissenberg number.

4.2. Necessity of the shifting particle technique

In this subsection, the 2D Taylor–Green flow[28] of the Newtonian fluid is simulated to show the necessity of the shifting particle technique.

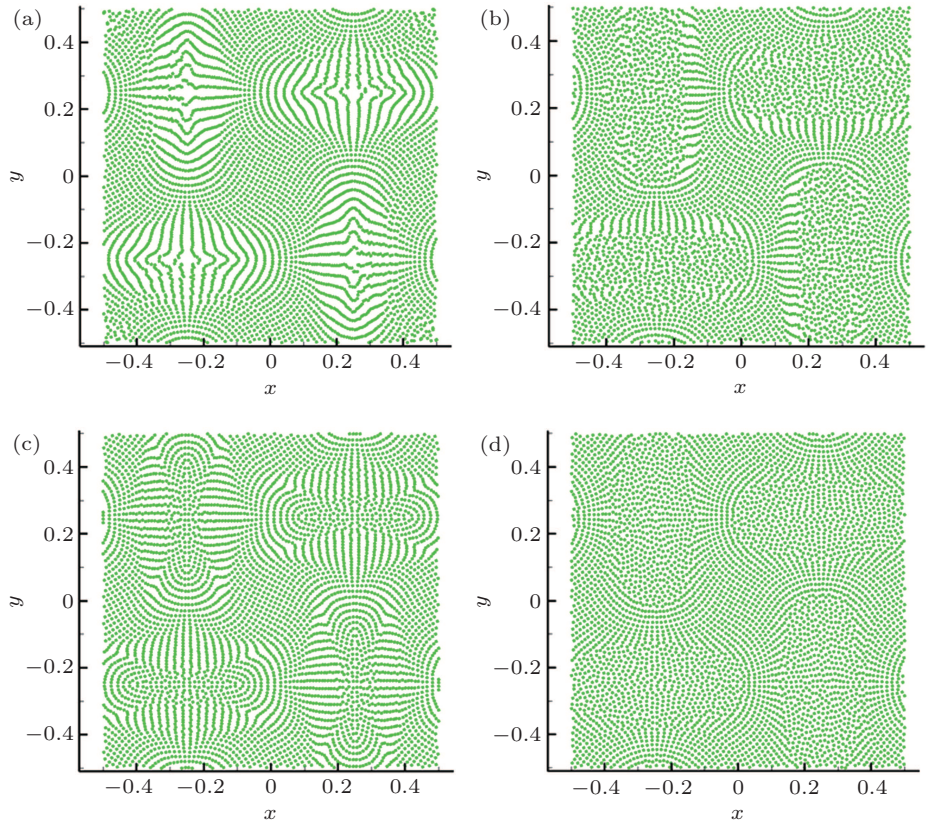


Fig. 3. (color online) Particle distributions obtained using different numerical methods with $Re = 100$, $t = 0.2$ s: (a) TSPH with cubic spline kernel; (b) TSPH with quintic Wendland kernel; (c) SPH_CS with quintic Wendland kernel; (d) SPH_CS_SP with quintic Wendland kernel.

The Taylor–Green flow is a periodic array of decaying vortices in the plane, and its velocity components are given

$$u = -U\,\mathrm{e}^{bt}\cos(2\pi x)\sin(2\pi y),$$
$$v = U\,\mathrm{e}^{bt}\sin(2\pi x)\cos(2\pi y), \tag{27}$$

where the velocity scale $U = 1$ m/s, the computational periodic domain $[0,1]\times[0,1]$, the kinematic viscosity $\upsilon_0 = 0.01$ m^2/s, Reynolds number $Re = UL/\upsilon_0 = 100$, and the decay rate of the velocity field $b = -8\pi^2/Re$.

Figure 3 shows the particle distributions for the Taylor–Green flow obtained by different numerical methods. It can be observed that the tensile instability in the TSPH results is more serious than that in other numerical results. The quintic Wendland kernel function has better stability than the conventional cubic spline kernel (Figs. 3(a) and 3(b)). The particle distributions obtained by SPH_CS_SP method are more uniform than those obtained by the TSPH method and SPH_CS method due to the effect of shifting particle technique combining with the corrected symmetric kernel gradient scheme and the quintic Wendland kernel function. Moreover, the tensile instability is much improved by the SPH_CS_SP method (Fig. 3(d)).

Figure 4 shows the velocity profiles at $x/L = 0.0$ with $Re = 100$, $t = 0.2$ s. The SPH_CS_SP results of velocity component $u(y)$ are much closer to the analytical solutions than the other numerical results, and small oscillations appear in the TSPH results.

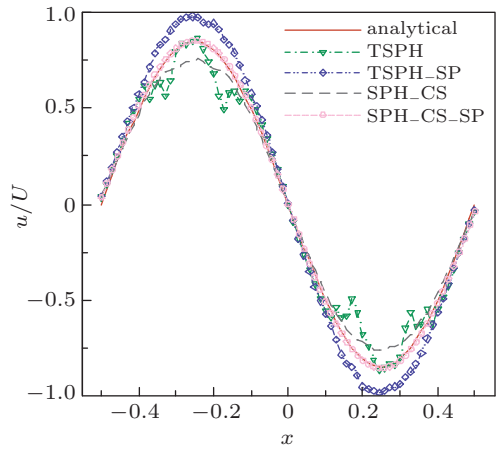


Fig. 4. (color online) Velocity profiles at $x/L = 0.0$ m with $Re = 100$, $t = 0.2$ s

The numerical results show that the proposed SPH_CS_SP method indeed has higher accuracy and better stability than the TSPH, TSPH_SP and SPH_CS method, and it is necessary to combine the shifting particles technique with the corrected symmetric kernel gradient scheme.

5. The reliability and the convergence of the SPH_CS_SP method

The polymer fluid flow around a periodic array of cylinders[30–32] is usually regarded as a challenging test for the particle method. Here, we use it to test the reliability of the proposed SPH_CS_SP method to simulate the viscoelastic fluid.

Figure 5 shows the geometric configuration of flow past a periodic array of cylinders and the analog configuration of single cylinder within a periodic lattice. The relevant parameters are as follows: F is an effective body force, r_c is the cylinder radius, L_H is the half height of two parallel channels, L_c is the distance between two neighbor cylinders, and x_c is the distance from the positive direction of x axis to the center of reference cylinder (see Fig. 5(b)). Some non-dimensional parameters are introduced: $Ro{=}x_c/r_c$, $L_r = L_c/r_c$, $Re = (\rho U r_c)/\eta$ and $We = (\lambda_{ob}U)/r_c$, $U' = u/10^{-km}$, $\tau'^{\alpha\beta} = \tau^{\alpha\beta}/10^{-km}$, $P' = p/10^{-kn}$ (where km and kn are the integers of scientific computing, $km = 4$, $kn = 3$ in these simulations), the first normal stress difference $N_1' = \tau'^{xx} - \tau'^{yy}$.

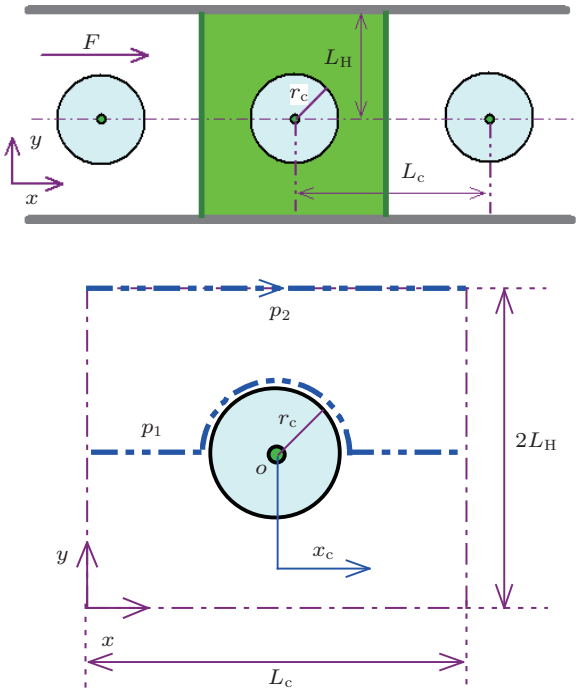


Fig. 5. (color online) Geometric configuration of flow past a periodic array of cylinders: (a) periodic array of cylinders; (b) analog configuration of a single cylinder.

5.1. Reliability test of numerical simulations

In order to test the reliability of the SPH_CS_SP method of simulating the flow past cylinders, the same example of Newtonian fluid as that in Ref. [9] is first simulated by the SPH_CS_SP method. All the physical parameters are the same as those in Ref. [9], i.e., $L_H = 0.05$ m, $r_c = 0.02$ m, $F = 5\times10^{-5}$ m·s^{-2}, $\rho = 10^3$ kg·m^{-3}, $\eta = 0.1$ Pa·s, $U = 1.5\times10^{-4}$ m·s^{-1}, $c = 0.01$ m·s^{-1}, and $Re = 0.03$; the fluid particles are uniformly distributed in the whole domain, and the particle number $N_y = 81$ along the y axis. The time step $\Delta t = 5\times10^{-3}$ s, smoothing length $h = 2.7d_0$.

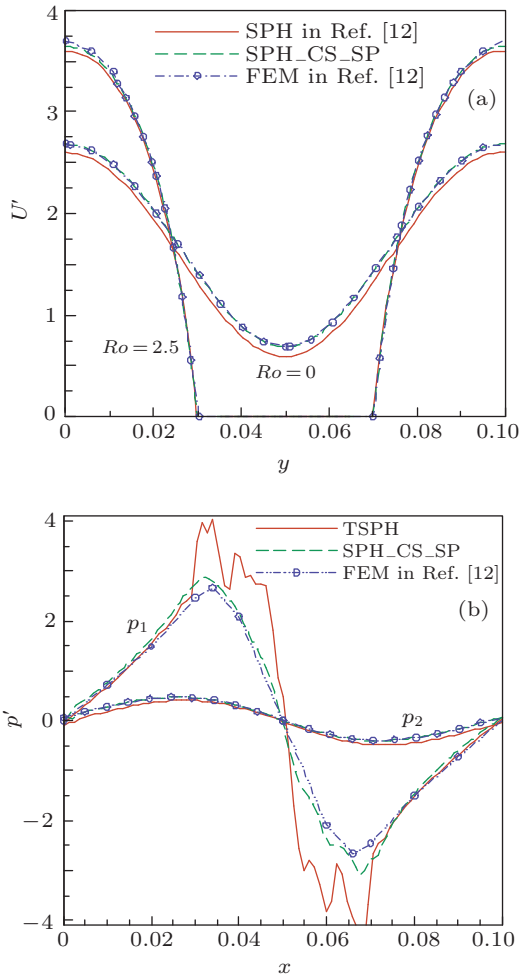


Fig. 6. (color online) Numerical results for the flow at stable state along different paths: (a) U; (b) pressure.

Figure 6 shows the curves of velocity U and the pressure at stable state along different paths (see Fig. 5(b)). It is worth noting that the fluid domain is not confined in Fig. 6, and the Newman boundary condition is enforced at the up and down boundary of the fluid domain. The SPH_CS_SP results are much closer to the FEM results than the TSPH and SPH results in Ref. [9], the pressure oscillation is more serious for the TSPH and SPH results in Ref. [9] than for the SPH_CS_CS results, which implies that the pressure oscillation can be well controlled by the SPH_CS_SP method.

Figure 7 shows the contours of velocity U and pressure obtained by the SPH_CS_SP method for the flow at the stable state under different boundary conditions (i.e., the flow is confined or not confined in a channel which corresponds to the Newman boundary condition or non-slip wall boundary condition, respectively). Comparing Fig. 7 with Fig. 12, Fig. 14 in Ref. [9] and Fig. 4 in Ref. [33], we can find that the numerical solutions obtained by the SPH_CS_SP method are always accurate and reliable.

In order to demonstrate the capacity of the SPH_CS_SP approach for simulating the viscoelastic flow past a periodic array of cylinders, the Oldroyd-B fluid flow past a periodic array of cylinders is simulated and the particle distribution at stable state is shown in Fig. 8. The employed physical quantities are as follows: $L_r = 6$, $L_{\mathrm{H}} = 0.04$ m, $U = 1.2 \times 10^{-4}$ m$\cdot$s^{-1}, $c = 0.02$ m$\cdot$s^{-1}, $Re = 0.024$, $We = 0.9$. $N_y = 71$, and $h = 2.7d_0$. The other parameters are the same as those in Fig. 6.

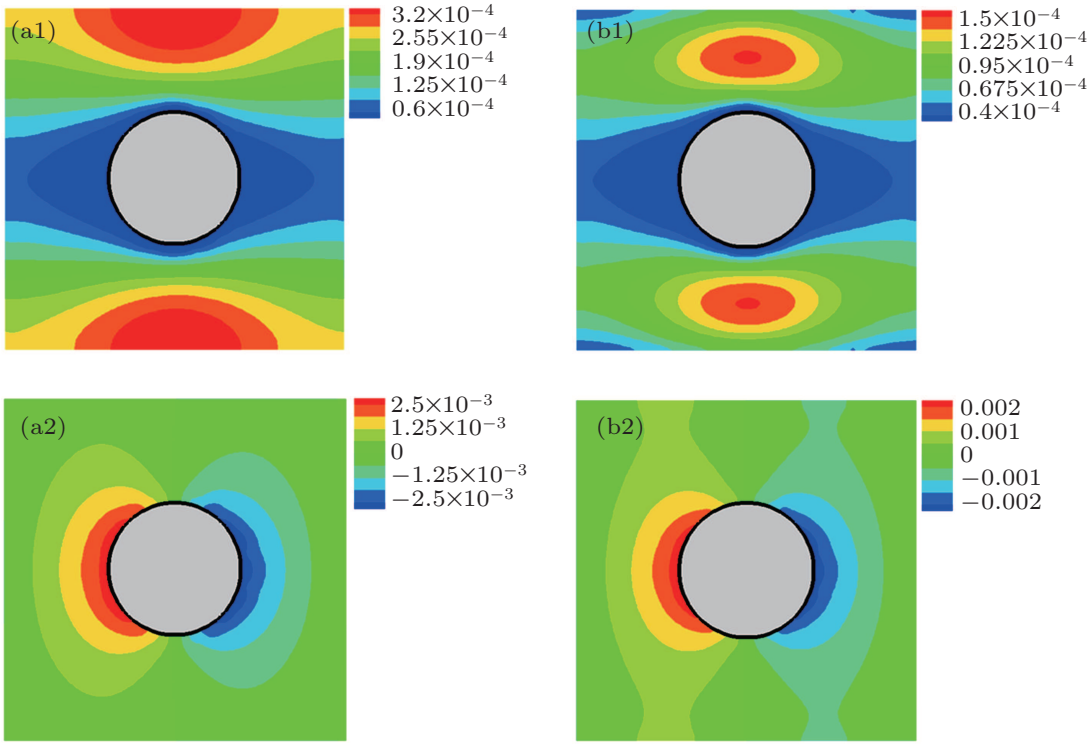


Fig. 7. (color online) Contour distributions of velocity U [(a1) and (b1)] and pressure [(a2) and (b2)] with different boundary conditions: (a1) and (a2) without confining a channel; (b1) and (b2) confined in a channel.

Moreover, the following drag[32] for the viscoelastic fluid flow past a cylinder is introduced, which is

$$F_D = 2\int_0^{2\pi} \Big[(-p+2\eta_s D^{xx}+\tau^{xx})\cos\theta + (2\eta_s D^{yy}+\tau^{yy})\sin\theta\Big]_{r=r_c} r_c\,\mathrm{d}\theta, \quad (28)$$

and the drag coefficient $C_D = F_D/(\eta U)$.

It can be seen that the so-called tensile instability appears near the cylinder in the SPH results (Fig. 8(a)), and can be improved by the SPH_CS_SP method (Fig. 8(b)).

From Figs. 6–8, we can conclude that the SPH_CS_SP method can credibly simulate the polymer flow around a periodic array of cylinders, and has higher accuracy and better stability than the TSPH method or SPH methods in Refs. [9] and [16].

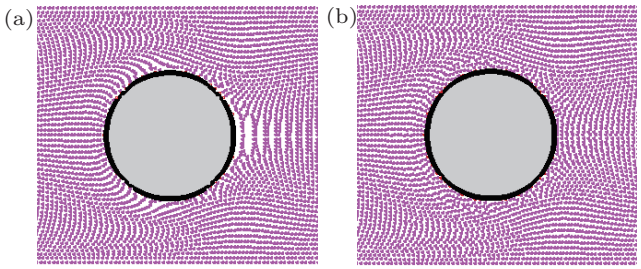


Fig. 8. (color online) Particle distributions at stable state for Oldroyd-B fluid flow past a periodic array of cylinders with $L_r = 6$, $We = 0.9$: (a) SPH in Ref. [22]; (b) SPH_CS_SP.

5.2. Numerical convergence analysis and drag coefficient calculation

According to Ref. [17], the numerical convergence of SPH scheme not only depends on the particle numbers, but also relies on the smoothing length. Next, the simple numerical convergence is investigated by increasing the particle number N_y with different values of smoothing length h.

Figure 9 shows the curves of velocity, shear elastic stress and first normal stress difference along different paths with increasing the particle number N_y at $L_r = 6$, $We = 0.06$, and L_{xy} represents the path over the cylinder centerline with the path being at 45° with respect to the horizontal line. It can be found that U, τ'^{xy}, and N_1' have good consistency with the increasing particle numbers, showing that the SPH_CS_SP method is convergent.

Figure 10 shows the shear elastic stresses along the path $Ro = 2$ with different values of smoothing length $h = 2.0d_0$, $2.4d_0$, $2.8d_0$, $L_r = 6$, $We = 0.8$, $\beta_0 = 0.2$. It can be found that the numerical results have good convergences at $h \geq 2.0d_0$ in our numerical simulations. Meanwhile, the tensile instability at $h = 2.4d_0$ is more serious than that at $h = 2.8d_0$. The analysis has shown good convergence for the proposed method at $h \geq 2.4d_0$.

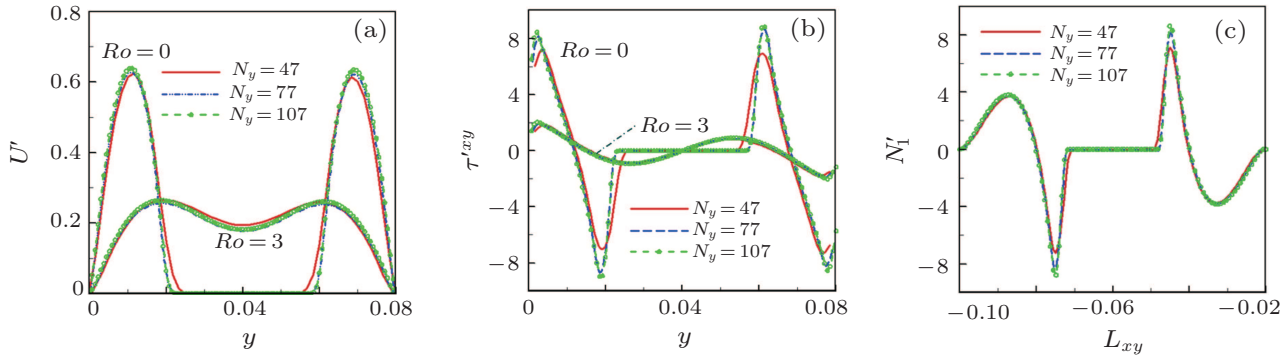


Fig. 9. (color online) Curves of velocity (a), shear elastic stress (b), and first normal stress difference (c) along different paths with increasing the particle number at $L_r = 6$ and $We = 0.06$.

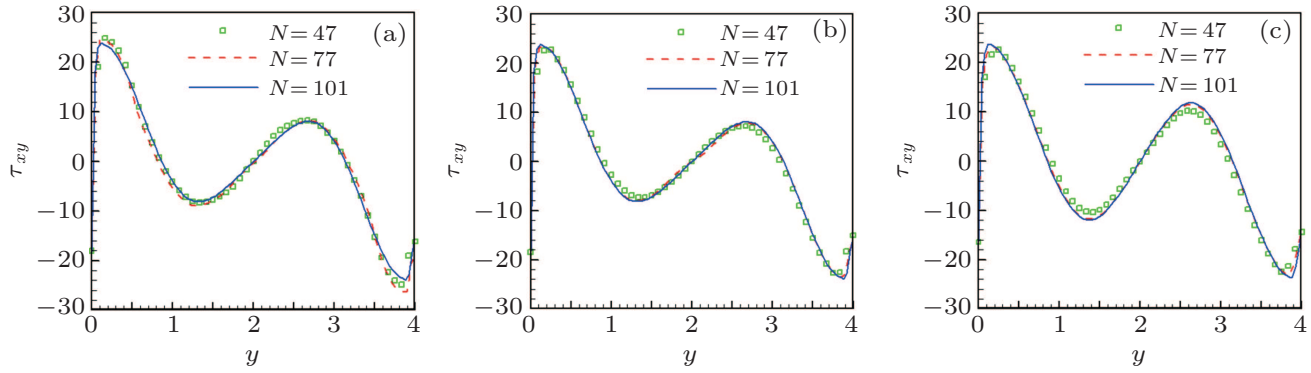


Fig. 10. (color online) Shear elastic stresses along the path $Ro = 2$ with different values of smoothing length h ($L_r = 6$, $We = 0.8$, $\beta_0 = 0.2$): (a) $h = 2.0d_0$; (b) $h = 2.4d_0$; (c) $h = 2.8d_0$.

Figures 11(a) and 11(b) show the variations of drag coefficient with the increasing particle number and Weissenberg number respectively. From Fig. 11(a), it can be seen that the drag coefficient for the Newtonian or Oldroyd-B fluid at $L_r = 6$ reaches a stable value with increasing N_y. The values of drag coefficient for the Newtonian fluid are nicely consistent with those in Refs. [31] and [32], the values of drag coefficient for the Oldroyd-B fluid are smaller than those for the Newtonian fluid. The change of the drag coefficient with $L_r = 6$ is more complex than that with $L_r = 2.5$ with increasing Weissenberg number (Fig. 11(b)), which is in agreement with the conclusion in Ref. [31]. In a word, the proposed SPH_CS_SP approach has desirable numerical convergence for simulating the problem of flow past a cylinder at low Reynolds number.

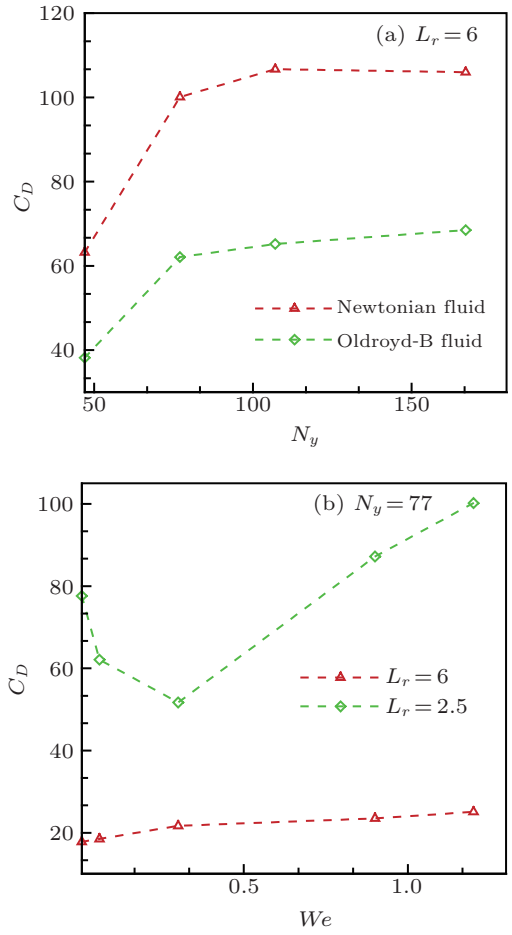


Fig. 11. (color online) Variations of drag coefficient with (a) N_y and (b) We.

6. Application of the SPH_CS_SP method to 3D viscoelastic free surface flows

In order to demonstrate the ability of the proposed particle method to capture the complex free surface in the true flow, the 3D viscoelastic jet bulking problem of filling process in a rectangle container is simulated by the SPH_CS_SP method with the MPI parallelization technique. In this section, the instability phenomenon of jet coiling based on the Oldroyd-B fluid is mainly simulated and predicted.

The geometry of 3D jet bulking is shown in Fig. 12. In this problem, the inflow boundary condition should be considered, which lies in the initial distribution of fluid particles before entering the container and the treatment of inlet velocity near the inflow boundary (Fig. 12). Here, the following inflow boundary treatment is adopted: (i) at the first time-step, many reserved fluid particles are uniformly distributed and away from the nozzle entry, and their injection velocity is equal to the inlet velocity; (ii) the profile sketch of reserving fluid particles takes on a disc shape for the injection process in a rectangle container (Fig. 12). In the simulations, the radius of inlet jet nozzle is r_c and the entry speed at the nozzle is U. The length, width and height of the rectangular container denote L_x, L_y and L_z, respectively. $Re = 2U\rho r_c/\eta$ is related to the viscosity of the fluid, and high value of Re corresponds to fluid with low viscosity. $We = \lambda_{0b}U/(2r_c)$ is related to the viscoelasticity of the fluid.

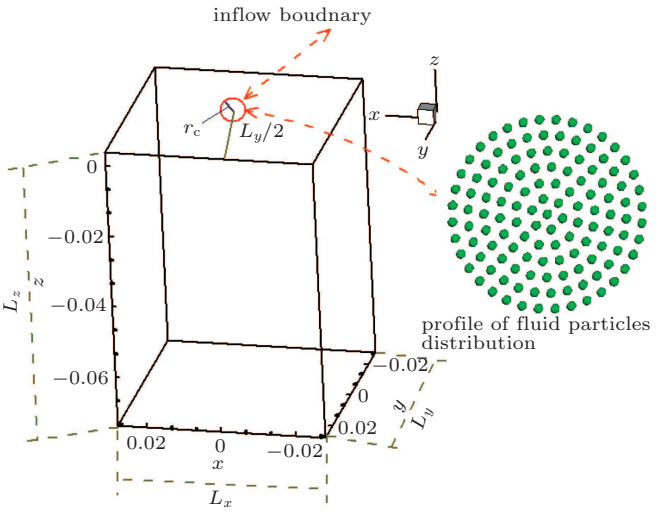


Fig. 12. (color online) Sketch of 3D jet bulking.

Figure 13 illustrates the instability phenomenon of jet coiling and w-velocity contour, and the jet coiling phenomenon of the Newtonian fluid is also shown for comparison. The parameters are as follows: the jet width $D = 5$ mm$(D = 2r_c)$, $L_x = L_y = 5$ cm, $L_z = 6$ cm, $U = -1\ \mathrm{m\cdot s^{-1}}$, $L_z/D = 12$, the reference density $\rho_0 = 1.1 \times 10^3\ \mathrm{k\cdot gm^{-3}}$, the gravitational acceleration $g_z = -9.81\ \mathrm{m\cdot s^{-2}}$, kinematic viscosity $\upsilon_0 = 0.02\ \mathrm{m^2\cdot s^{-1}}$, speed of sound $c = 8\ \mathrm{m\cdot s^{-1}}$, $\beta_0 = 0.4$, $\lambda_{0b} = 0.005$ s $(We = 1)$, $\lambda_{0b} = 0.5$ s $(We = 100)$, $Re = 0.25$, and the time-step $\Delta t = 10^{-6}$ s.

According to previous research,[34,35] the phenomenon of jet coiling based on the Newtonian fluid will occur, if $Re < 0.5$ and $L_z/D > 10$ or $Re < 1.2$ and $L_z/D > 7$ are satisfied. From Fig. 13, we can see that the jet coiling indeed occurs for the Newtonian fluid with $Re = 0.25$ and $L_z/D = 12$, the reason can be explained as follows. On the one hand, the effect of

the viscous force on flow is much bigger than that of inertia force after the fluid has touched the solid plate, thereby leading to the slow flow of the fluid. On the other hand, the fluid is continuously injected from the nozzle. The results of instability phenomenon of jet coiling based on the Oldroyd-B fluid basically are consistent with those obtained by FDM with MAC method in Refs. [30] and [35]. Also, the absolute value of w-velocity near the front of jet fluid is bigger than that of the inlet velocity before the jet fluid reaches the bottom of rectangle container ($t = 0.027$ s). Thus the required time for Oldroyd-B fluid to arrive at the bottom of the rectangular container is shorter than that for Newtonian fluid, and the jet coiling phenomenon of the Oldroyd-B fluid lags behind that of Newtonian fluid due to the shear thinning behavior of the Oldroyd-B fluid, which reduces the viscosity when subjected to shear strain and is the unique characteristic of the non-Newtonian fluid. The w-velocity of the front of the jet fluid increases then decreases with time going by. Comparing Fig. 13 with the numerical results in Refs. [30], [34], and [35], we can obtain the conclusion that it is credible for the SPH_CS_SP method to simulate the 3D viscoelastic free surface flows.

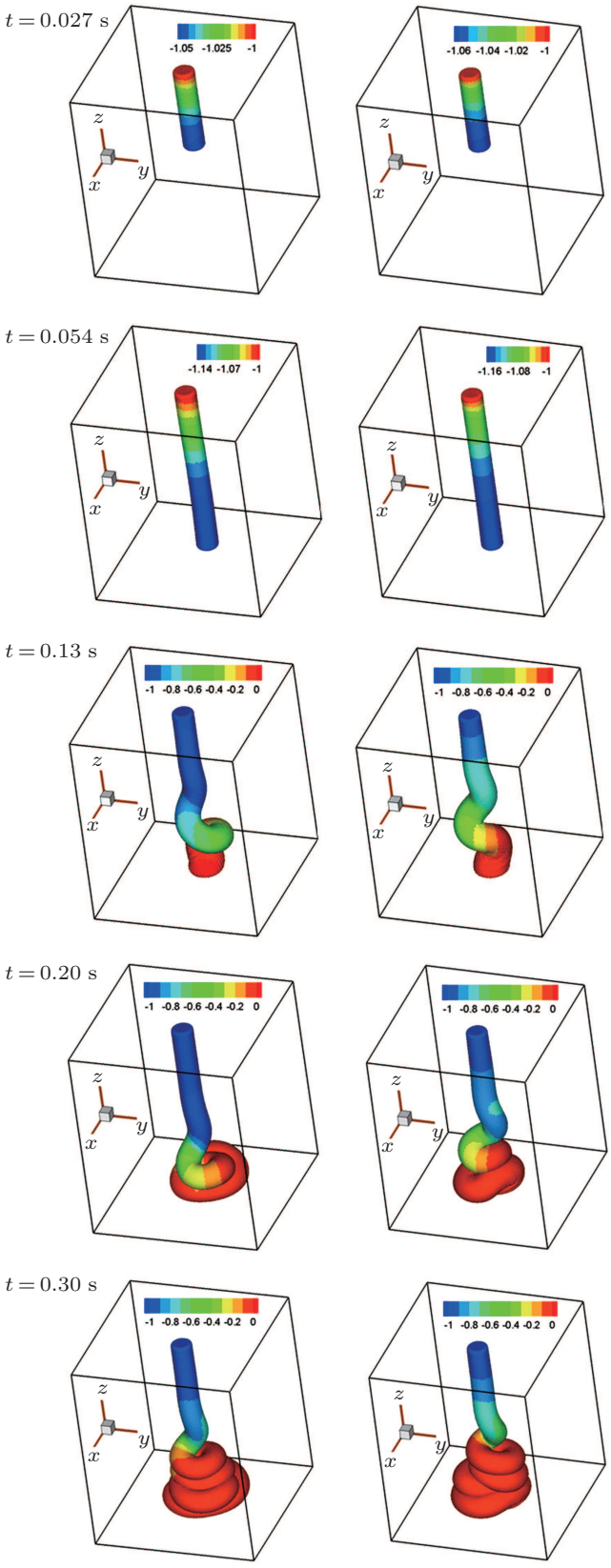


Fig. 13. (color online) The flow and w-velocity contours of the jet bulking based on the Newtonian (first column) and Oldroyd-B (second column) fluid with $Re = 0.25$ and $We = 1$.

In order to clearly show the instability phenomenon of jet coiling, figure 14 displays the deformation processes of the center line of the jet based on the Newtonian fluid and Oldroyd-B fluid, which correspond to the results in Fig. 13 except for the results with $We = 100$. It can be seen that the jet coiling phenomenon indeed occurs which is more obvious than that in Fig. 13.

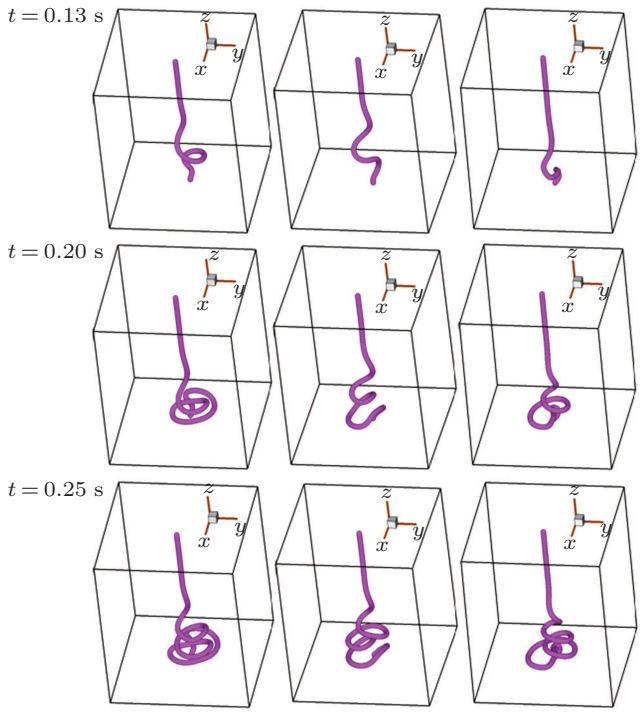


Fig. 14. (color online) Deformation processes of the center line of jet with $Re = 0.25$: Newtonian fluid (first column); Oldroyd-B fluid with $We = 1$ (second column), and $We = 100$ (third column).

Next, the influences of macroscopic rheological parameters on the fluid deformation of filling process are predicted

and discussed to further illustrate the complex phenomenon in the 3D viscoelastic filling process.

6.1. Influence of *We*

Observing Fig. 14, we can easily find that *We* has an important effect on the deformation process of viscoelastic jet fluid, and the phenomenon of jet coiling may occur for higher *We* at lower Reynolds number (*We*=100 in Fig. 14).

To further demonstrate the influence of *We* on the deformation process of jet coiling, we investigate the fluid deformations and the jet lengths of the jet buckling for the Oldroyd–B fluid with different Weissenberg numbers at *Re*=0.6. Here the jet length is defined as the distance from the jet front to the nozzle. The employed parameters are as follows: $D = 6$ mm, $L_x = \quad L_y = 6$ cm, $L_z = 5$ cm ($L_z/D = 8.3$), $U = -0.5\ \mathrm{m\cdot s^{-1}}$, $\Delta t = 5 \times 10^{-6}$ s, $\upsilon_0 = \eta/\rho_0 = 0.005\ \mathrm{m^2\cdot s^{-1}}$ ($Re = 0.6$), $\lambda_{0\mathrm{b}} = 0.006$ s ($We = 1$), $\lambda_{0\mathrm{b}} = 0.03$s ($We = 5$), $\lambda_{0\mathrm{b}} = 0.6$s ($We = 100$), and the other parameters are the same as those in Fig. 13. The results are shown in Fig. 15.

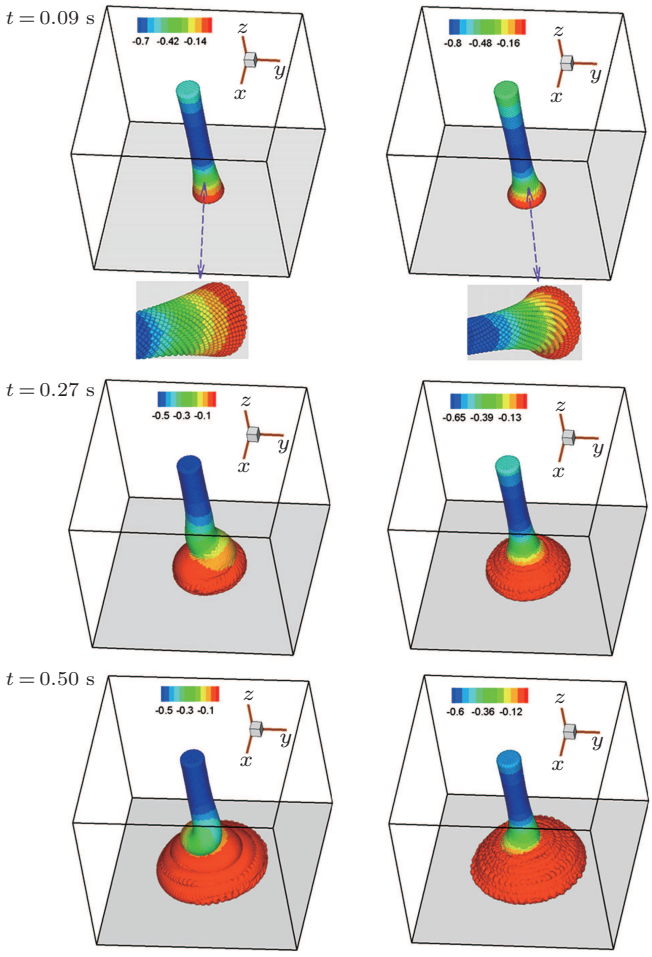


Fig. 15. (color online) Filling deformation processes based on the Oldroyd-B fluid with $Re = 0.6$, $We = 1$ (first column) and 100 (second column) at different times.

From Fig. 15, we can find that the instability phenomenon of jet coiling appears with *We*=1 at $t = 0.5$s, but it does not occur when *We* changes from 1 to 100 due to the effect of elastic stress and shear thinning. The reason is that moreover, the forefront of the jet fluid is warped as the jet coiling happens, which may be obviously observed from Fig. 15 at the initial stage of jet fluid impacting on the container bottom (at $t = 0.09$ s). The warped distortion of jet fluid may be another reason for generating the instability phenomenon of jet coiling, which was not mentioned in previous studies.[30,34,35]

Figure 16 shows the variations of jet length of the jet bulking with time for different values of Weissenberg numbers. It can be observed that a longer jet length is achieved at a higher Weissenberg number. The reason is explained as follows. The increasing of *We* indicates that the relaxation time of the fluid increases, now the shear thinning character of the fluid instead of the elasticity dominates the flow in a short time before the fluid retracts. The conclusion is consistent with the remarks in Refs. [30] and [35].

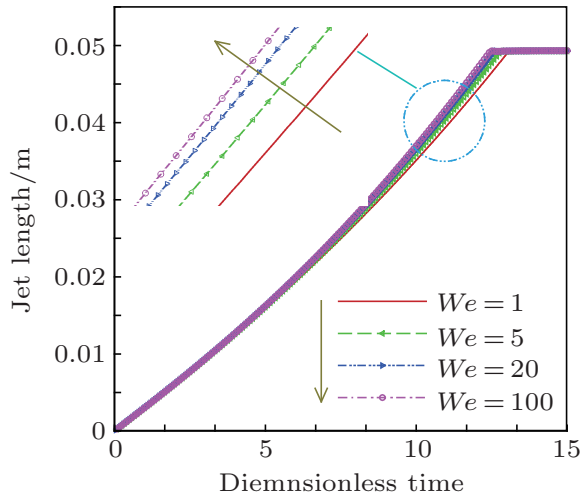


Fig. 16. (color online) Variations of jet length of jet bulking with time for different values of *We*.

6.2. Influence of *Re*

Another macroscopic parameter which has an important influence on the deformation of jet fluid is the Reynolds number. Comparing Fig. 13 with Fig. 15, it is easy to find that the jet coiling phenomenon is weak as the Reynolds number increases.

In order to further show the effect of the Reynolds number on the viscoelastic flow, figure 17 displays the deformation processes of the jet buckling for the Oldroyd-B fluid with *Re*=1, 5, and 10. The parameters are as follows: $D = 8$ mm, $L_x = L_y = 8$ cm, $L_z = 6$ cm ($L_z/D = 7.5$), $U = -0.5\ \mathrm{m\cdot s^{-1}}$, $\lambda_{0\mathrm{b}} = 0.006$ s ($We = 1$), $\upsilon_0 = 0.004\ \mathrm{m^2\cdot s^{-1}}$ ($Re = 1$), $\upsilon_0 = 0.0008\ \mathrm{m^2\cdot s^{-1}}$ ($Re = 5$), $\upsilon_0 = 0.0004\ \mathrm{m^2\cdot s^{-1}}$ ($Re = 10$), and the other parameters are the same as those in Fig. 15.

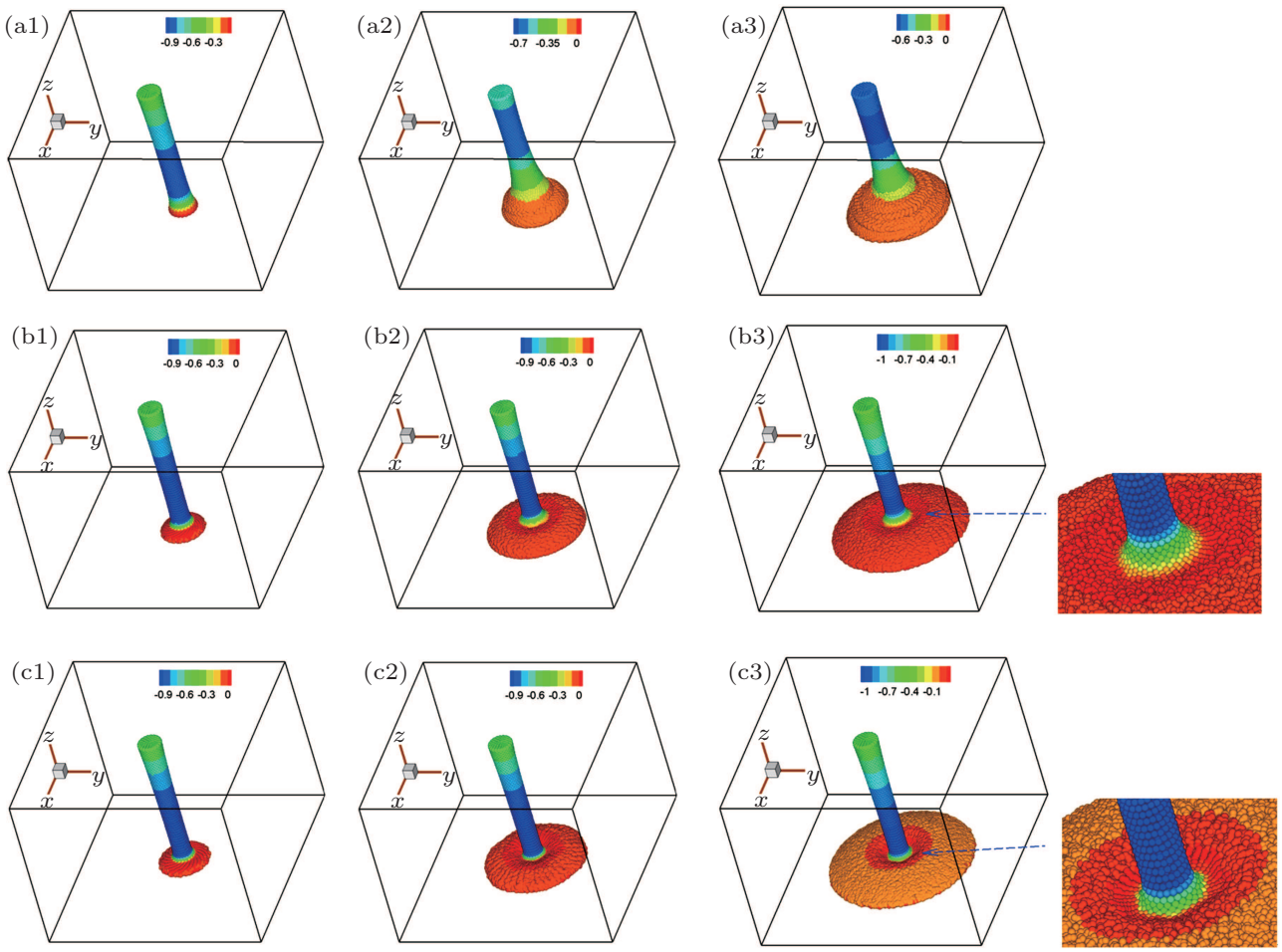


Fig. 17. (color online) Deformation processes of jet buckling of the Oldroyd-B fluid at different times ($t = 0.09$ s, $t = 0.21$ s, $t = 0.039$ s) with different Reynolds numbers: $Re = 1$ ((a1)–(a3)), 5 ((b1)–(b3)), and 10 ((c1)–(c3)).

From Fig. 17, we can find that the filling processes are stable at Re=1 (Figs. 17(a1)–17(a3)), which is required in the industrial manufacture. The phenomenon of jet coiling disappears as the Reynolds number continues to increase until$Re \geq 1$. As the Reynolds number increases up to 5 or 10, the concave phenomenon of forefront fluid appears as the jet fluid impacts on the container bottom (Figs. 17(b3)–17(c3)). The more serious concave tendency is achieved as the Reynolds number increases (Figs. 17(b3)–17(c3)). The concave phenomenon of jet fluid is unstable, which will generate some gas bubbles in the filling process.

7. Conclusions

In this work, the flow behavior of 3D jet buckling problem based on the Oldroyd-B model is simulated and predicted by a corrected particle scheme (SPH_CS_SP) method. The accuracy of the SPH_CS_SP method and the necessity of the shifting particle technique are first verified by two benchmark problems, that is, the Poiseuille flow and Taylor–Green flow, respectively. Then, the validity of the proposed SPH_CS_SP method to simulate the viscoelastic free surface is shown by the polymeric fluid flow around a periodic array of cylinders. Finally, the present method with MPI parallelization technique is further used to simulate the 3D jet coiling problem of filling process. The influences of macroscopic parameters on the instability phenomena are also investigated. Some conclusions can be drawn from the numerical results below.

(I) The SPH_CS_SP method has better robustness and higher accuracy than the TSPH, the particle clustering phenomenon can be well eliminated by the SPH_CS_SP method. The pressure distributions obtained by the SPH_CS_SP are much smoother than those obtained by TSPH method and other SPH methods.

(II) The SPH_CS_SP method can effectively and accurately simulate the 3D viscoelastic free surface flows.

(III) The jet coiling problem for the Oldroyd-B fluid is more complex than that for the Newtonian fluid. The macroscopic parameters We and Re have an important influence on the deformation process of polymer jet coiling. The phenomenon of jet coiling is weakened as We or Re increases, more serious concave phenomenon of jet fluid occurs as Re increases.

References

[1] Owens R G and Phillips T N 2002 *Computational Rheology* (London: Imperial College Press) p. 1
[2] Cleary P W and Monaghan J J 1999 *J. Comput. Phys.* **148** 227
[3] Feng Z, Wang X D and Ouyang J 2013 *Chin. Phys. B* **22** 074704
[4] Chen F Z, Qiang H F and Gao W R 2014 *Acta Phys. Sin.* **63** 130202 (in Chinese)
[5] Gingold R A and Monaghan J J 1997 *Mon. Not. R. Astron. Soc.* **181** 375
[6] Liu W K, Jun S and Zhang Y F 1995 *Int. J. Numer. Method Fluids* **20** 1081
[7] Li S F and Liu W K 1999 *Int. J. Numer. Method Eng.* **45** 251
[8] Li S F and Liu W K 1999 *Int. J. Numer. Method Eng.* **45** 251)
[9] Morris J P, Fox P J and Zhu Y 1997 *J. Comput. Phys.* **136** 214
[10] Fang J, Parriaux A, Rentschler M and Ancey C 2009 *Appl. Numer. Math.* **59** 251
[11] Liu M B and Liu G R 2010 *Arch. Comput. Method Eng.* **17** 25
[12] Hu X Y and Adams N A 2007 *J. Comput. Phys.* **227** 264
[13] Shao S and Lo EYM 2003 *Adv. Water Resour.* **26** 787
[14] Hu X Y and Adams N A 2006 *J. Comput. Phys.* **213** 844
[15] Ellero M and Tanner R I 2005 *J. Non-Newtonian Fluid Mech.* **132** 61
[16] Liu M B and Liu G R 2006 *Appl. Numer. Math.* **56** 19
[17] Quinlan N J, Basa M and Lastiwka M 2006 *Int. J. Numer. Method Eng.* **66** 2064
[18] Monaghan J J 2000 *J. Comput. Phys.* **159** 290
[19] Chen J K and Beraun J E 2000 *Comput. Methods Appl. Mech. Engrg.* **190** 225
[20] Liu M B, Xie W P and Liu G R 2005 *Appl. Math. Model.* **29** 1252
[21] Zhang G M and Batra R C 2007 *J. Comput. Phys.* **222** 374
[22] Zhang G M and Batra R C 2009 *Comput. Mech.* **43** 321
[23] Bonet J and Lok T S L 1999 *Comput. Methods Appl. Mech. Engrg.* **180** 97
[24] Oger G, Doring M, Alessandrini B and Ferrant P 2007 *J. Comput. Phys.* **225** 1472
[25] Shadloo M S, Zainali A, Yildiz M and Suleman A 2012 *Int. J. Numer. Method Eng.* **89** 939
[26] Basa M, Quinlan N J and Lastiwka M 2009 *Int. J. Numer. Method Fluids* **60** 1127
[27] Ren J L, Ouyang J, Jiang T and Li Q 2012 *Comput. Mech.* **49** 643
[28] Xu R, Stansby P and Laurence D 2009 *J. Comput. Phys.* **228** 6703
[29] Wendland H 1995 *Adv. Comput. Math.* **4** 389
[30] Tomé M F, Castelo A, Ferreira V G and McKee S 2008 *J. Non-Newtonian Fluid Mech.* **154** 179
[31] Liu A W, Bornside D E, Armstrong R C and Brown R 1998 *J. Non-Newtonian Fluid Mech.* **77** 153
[32] Ellero M andAdams N 2011 *Int. J. Numer. Method Eng.* **86** 1027
[33] Vazquez-Quesada A, Ellero M 2012 *J. Non-Newtonian Fluid Mech.* **167–168** 1
[34] Tomé M F, Grossi L, Castelo A, Cuminato J A, Mangiavacchi N, Ferreira V G, Sousa F S de and McKee S 2004 *J. Non-Newtoian Fluid Mech.* **123** 85
[35] Oishi C M, Tomé M F, Cuminato J A and McKee S 2008 *J. Non-Newtoian Fluid Mech.* **227** 7446